

JGR Space Physics



RESEARCH ARTICLE

10.1029/2021JA030170

Key Points:

- First simultaneous observations of the Ni and Na layers over a full annual cycle, which are simulated well by a whole atmosphere model
- Both metal layers peak in midwinter with roughly three times the abundance of their midsummer minima
- The Ni layer is displaced about 8 km below the Na layer, which is explained by significant differences in their neutral and ion chemistry

Correspondence to:

J. Plane and G. Yang,
j.m.c.plane@leeds.ac.uk;
gyang@nssc.ac.cn

Citation:

Jiao, J., Feng, W., Wu, F., Wu, F., Zheng, H., Du, L., et al. (2022). A Comparison of the midlatitude nickel and sodium layers in the mesosphere: Observations and modeling. *Journal of Geophysical Research: Space Physics*, 127, e2021JA030170. <https://doi.org/10.1029/2021JA030170>

Received 1 DEC 2021
 Accepted 25 JAN 2022






Author Contributions:

Conceptualization: Jing Jiao, Guotao Yang, John Plane
Data curation: Jing Jiao, Wuhu Feng
Formal analysis: Jing Jiao, Wuhu Feng, Fang Wu, Fujun Wu, Haoran Zheng, Lifang Du, Guotao Yang, John Plane
Funding acquisition: Guotao Yang, John Plane
Investigation: Jing Jiao, Wuhu Feng, Fang Wu, Fujun Wu, Haoran Zheng, Lifang Du
Methodology: Wuhu Feng
Project Administration: Guotao Yang, John Plane
Resources: Guotao Yang
Software: Wuhu Feng
Supervision: Guotao Yang
Validation: Lifang Du

©2022. The Authors.

This is an open access article under the terms of the [Creative Commons Attribution License](https://creativecommons.org/licenses/by/4.0/), which permits use, distribution and reproduction in any medium, provided the original work is properly cited.

A Comparison of the Midlatitude Nickel and Sodium Layers in the Mesosphere: Observations and Modeling

Jing Jiao¹ , Wuhu Feng^{2,3} , Fang Wu^{1,4} , Fujun Wu^{1,4}, Haoran Zheng¹, Lifang Du¹, Guotao Yang¹ , and John Plane² 

¹National Space Science Center, State Key Laboratory of Space Weather, Chinese Academy of Sciences, Beijing, China, ²School of Chemistry, University of Leeds, Leeds, UK, ³National Centre for Atmospheric Science, University of Leeds, Leeds, UK, ⁴University of Chinese Academy of Sciences, Beijing, China

Abstract A dual-wavelength resonance fluorescence lidar facility, operating at 341 and 589 nm, was used to observe simultaneously the Ni and Na layers in the upper atmosphere over Yanqing station, Beijing (40.41°N, 116.01°E). Lidar measurements were performed on 126 nights (1090 hr in total) from April 2019 to March 2020 and April 2021 to August 2021, so that the full seasonal cycle of the Ni layer was observed for the first time. The Ni and Na layers exhibit a similar annual cycle, increasing by a factor of ~3 from a mid-summer minimum to a midwinter maximum. The annual mean column densities of Ni and Na are 3.1×10^8 and 2.5×10^9 cm⁻², respectively, giving a mean Na:Ni ratio of 8.1, which is significantly larger than their CI chondritic ratio of 1.2. This is explained by the more efficient ablation of Na from cosmic dust particles by a factor of 3, and the more rapid neutralization of Na⁺ between 90 and 100 km, where the measured Na⁺:Ni⁺ ratio is only 2.2. The Ni layer peak occurs around 84 km, 8 km below that of Na. These features are simulated satisfactorily by the Whole Atmosphere Community Climate Model (WACCM) and are explained by significant differences in the neutral chemistry of the two metals below 90 km and their ion-molecule chemistry between 90 and 100 km.

Plain Language Summary Layers of metal atoms are produced in the upper atmosphere by the ablation of cosmic dust particles, which enter the atmosphere at hyperthermal speeds, so that a significant fraction of them melt and evaporate. A layer of sodium atoms has been observed for more than 40 years both from the ground and space. In contrast, a layer of nickel atoms was only discovered 6 years ago. Ni is of interest because it occurs in an iron-nickel-sulfide phase in cosmic dust, whereas sodium occurs in the bulk metal silicate phase. Also, the Ni layer extends lower in the atmosphere than the other metals, such as Na, Fe, and Mg. This study reports the first observations of the seasonal behavior of Ni along with simultaneous Na measurements. Although the seasonal behavior of the two metals is similar (maximum in winter and minimum in summer), the Ni layer peaks 8 km below the Na layer as a result of important differences in the atmospheric chemistry, which controls the layers. There is about 8 times as much Na as Ni compared with a ratio of 1.2 in carbonaceous meteorites. All these features are simulated satisfactorily by a global chemistry-climate model.

1. Introduction

The layer of nickel (Ni) atoms in the upper mesosphere and lower thermosphere (MLT) as well the layers of other metals (Fe, Na, Mg, Ca, and K) produced by meteoric ablation provide a unique means of observing the physics and chemistry of the atmosphere between 75 and 110 km (Plane, 2003; Plane et al., 2015). Although the Ni layer was only observed for the first time in 2012 (Collins et al., 2015), much progress in understanding the characteristic features of the layer has been made in the past 5 years. This has been achieved through a combination of further observations (Gerding et al., 2019; Wu et al., 2021), laboratory studies of relevant physicochemical parameters (Bones et al., 2019, 2020; Daly et al., 2020; Mangan et al., 2019), and atmospheric modeling (Carrillo-Sánchez et al., 2020; Daly et al., 2020).

Measurements of the atomic Ni layer were first made at Chatanika, Alaska (65°N, 147°W), on two nights in midwinter 2012 by using lidar to probe the Ni (³F₄ – ³D) transition at $\lambda_{\text{air}} = 336.96$ nm (Collins et al., 2015). The peak density was reported to be 1.6×10^4 cm⁻³ at 87 km with a column abundance of 2.7×10^{10} cm⁻². Surprisingly, the Fe:Ni column abundance ratio was only 1.2, which is much smaller than the carbonaceous Ivuna (CI) chondritic ratio of 18 (Asplund et al., 2009). This result prompted a further lidar study during six

Writing – original draft: Jing Jiao, John Plane
Writing – review & editing: Wuhu Feng, John Plane

nights between January and March 2018 at Kühlungsborn in Germany using the same spectroscopic transition as Collins et al. (2015), as well as the stronger Ni($a^3D_3 - ^3F_4$) transition at $\lambda_{\text{air}} = 341.48$ nm (Gerding et al., 2019). The Ni densities were found to be much lower with peak densities ranging from 280 to 450 cm^{-3} and column abundances from $(3.1\text{--}4.9) \times 10^8 \text{ cm}^{-2}$. The implied Fe:Ni ratio of 38 is a factor of 2 larger than the CI ratio.

The very large discrepancy between the results from Chatanika and Kühlungsborn stimulated a further Ni lidar study over 25 nights between April and December 2019 at Yanqing, China (40.41°N, 116.01°E) (Wu et al., 2021). This study reported that the Ni peak density ranged from 98 to 460 cm^{-3} with a peak altitude between 80 and 88 km. The average peak density of $258 \pm 115 \text{ cm}^{-3}$ and the Ni column abundance, which varied from $(1.5\text{--}6.0) \times 10^8 \text{ cm}^{-2}$ between midsummer and midwinter, is in good agreement with the earlier Kühlungsborn result (Gerding et al., 2019). One standout feature that all three studies agree on is that the underside of the Ni layer profile is significantly broader than that of the Fe layer, often extending to below 80 km (Collins et al., 2015; Gerding et al., 2019; Wu et al., 2021).

These observations were complemented by two types of experimental work on Ni in the laboratory at Leeds. First, the rate of ablation of Ni from meteoritic fragments was measured under conditions of atmospheric entry using the Meteoric Ablation Simulator (MASI) (Bones et al., 2019). The results were then used to develop a new version of the Leeds Chemical Ablation Model (CABMOD-3), where the Ni is hosted in Ni-Fe-S grains separate from the bulk Fe-Mg-SiO₄ phase (Carrillo-Sánchez et al., 2020). The Meteoric Input Function (MIF) of Ni is the injection rate of Ni as a function of height in the atmosphere. This was estimated by combining CABMOD-3 with the Zodiacal Cloud Model (ZoDy) (Nesvorný et al., 2011), which provides the mass, velocity, and radiant distributions for cometary and asteroidal particles in the near-Earth environment (Carrillo-Sánchez et al., 2020).

The second type of experimental work was a series of kinetic studies of the relevant neutral (Daly et al., 2020; Mangan et al., 2019) and ion-molecule (Bones et al., 2020) chemical reactions that Ni-containing species are likely to undergo in the MLT. This work was supplemented by estimating the rate coefficients of other pertinent reactions that could not be measured using quantum theory calculations combined with semiempirical rate theory (Daly et al., 2020). The important neutral and ion-molecule chemistry of Ni is discussed below in Section 4.

The first global atmospheric model of Ni (WACCM-Ni) incorporated the Ni MIF and a comprehensive set of 43 neutral, ion-molecule, and photochemical reactions involving Ni species into a chemistry-climate model, the Whole Atmospheric Community Climate Model (WACCM6) (Daly et al., 2020). The model was able to reproduce satisfactorily the late winter/early spring Ni layer measured over 6 nights at Kühlungsborn (Gerding et al., 2019) as well as earlier rocket-borne mass spectrometric measurements of Ni⁺ ions (Daly et al., 2020). WACCM-Ni also predicted that the Ni column abundance would exhibit a wintertime maximum and a summertime minimum at 40°N, varying by a factor of ~ 3 (Daly et al., 2020).

In contrast to Ni, the Na layer has been observed for over 40 years (Plane, 2003). Knowledge of its seasonal variation has been obtained at several latitudes by long-term lidar observations (Gardner et al., 2005; Megie & Blamont, 1977; She et al., 2000; Simonich et al., 1979; States & Gardner, 1999) and near-globally by spaceborne spectroscopy (Fan et al., 2007; Fussen et al., 2010; Langowski et al., 2017). At midlatitudes near 40°N, the Na column abundance exhibits a strong annual variation by a factor of ~ 3 with a maximum in midwinter and a minimum in midsummer. The Na layer has also been satisfactorily modeled by WACCM-Na (Dunker et al., 2015; Feng et al., 2017; Langowski et al., 2017; Li et al., 2018; Marsh et al., 2013; Yuan et al., 2019).

In this paper, we report for the first time the seasonal and nocturnal variations of the mesospheric Ni at midlatitudes, measured over the past two years at the Yanqing lidar station near Beijing (40°N, 116°E). The characteristic features of the layer are contrasted with those of the Na layer, which were observed simultaneously. This data set is also compared with simulations of the WACCM-Ni and WACCM-Na models, thereby providing a rigorous test of our current understanding of the atmospheric chemistry of these two meteoric metals.

2. Data and Methods

2.1. The Na-Ni Lidar

The lidar system at Yanqing is designed to observe the Ni and Na layers simultaneously. The system consists of a transmitter unit, receiver unit, data acquisition unit, and an automatic control unit. These are shown schematically in Figure 1. A pulsed 532 nm Nd:YAG laser (optically pumped using flashtubes) is used to pump two pulsed dye

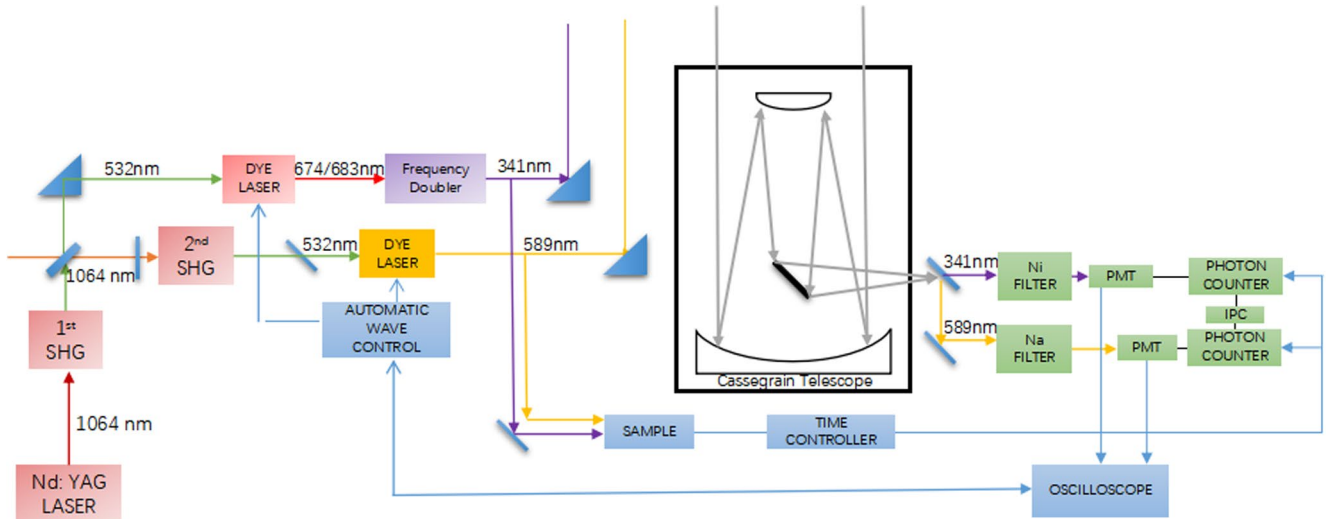


Figure 1. Schematic diagram of Beijing Na-Ni lidar system. SHG = second harmonic generator; PMT = photomultiplier tube.

lasers used for the Na and Ni layer detection. The repetition rate of the Nd:YAG laser is 30 Hz. One dye laser excites the Na resonance fluorescence transition at 589 nm (Jiao et al., 2015). The second is frequency-doubled to produce light at 341 nm with an average pulse energy of ~ 30 mJ, which is used for Ni resonance fluorescence scattering (Wu et al., 2021). A 1200-mm-diameter Cassegrain telescope, coupled with the receiver unit (optical filters, photomultiplier tubes, and photon counters), detects Rayleigh scattering from air molecules and resonant fluorescence scattering from the Ni and Na layers.

The Ni or Na densities at altitude z are calculated using the standard lidar equation:

$$n_{Mt}(z) = n_A(z_R) \frac{N_{Mt}(z) - N_B}{N_R(z_R) - N_B} \frac{Z^2 \sigma_R}{Z_R^2 \sigma_{Mt}}, Mt = Ni \text{ or } Na \quad (1)$$

where $N_{Mt}(z)$ is the resonance count rate of Na or Ni atoms, $N_R(z_R)$ is the Rayleigh count rate at the reference altitude, N_B is the background count rate, $n_A(z_R)$ is the air density at the reference altitude taken from NRLM-SISE-00 (Picone et al., 2002), and (z_R) is the reference altitude chosen as 50 km for the Ni layer (that is, avoiding corrections for stratospheric aerosol backscatter and ozone absorption) and 30 km for the Na layer. The effective differential backscatter cross sections are calculated as described by Chu and Papen (2005). The laser linewidth for Na is 1.5 and 0.95 GHz for Ni. This yields $\sigma_R = 4.4 \times 10^{-31} m^2 sr^{-1}$ and $\sigma_{Ni} = 1.419 \times 10^{-17} m^2 sr^{-1}$ for Rayleigh and resonance backscatter at 341 nm, respectively. For Rayleigh and resonance backscatter at 589 nm, $\sigma_R = 4.14 \times 10^{-32} m^2 sr^{-1}$ and $\sigma_{Na} = 5.22 \times 10^{-16} m^2 sr^{-1}$. The Na-Ni lidar recorded data with a temporal resolution of 33 s and a vertical height resolution of 96 m.

The initial measurements of the Ni layer made by this lidar were analyzed by Wu et al. (2021): for 25 nights of measurements, the Ni peak density ranged from 98 to 460 cm^{-3} with the peak altitude between 80 and 88 km. In the present paper, this initial data set is substantially increased: from April 2019 to March 2020 and April 2021 to August 2021, we obtained 1090 hr of Ni and Na number density data, covering 126 nights of observations at Yanqing. Figure 2 shows the statistics of the observational hours and nights as a function of month. Data in different years are folded into a single year according to the day number of the observation. Fewer measurements were made in summer due to the prevailing cloudy/rainy weather.

2.2. The WACCM-Ni/Na Models

The global atmospheric model WACCM-Ni (Daly et al., 2020) is outlined in Section 1. The version of the Whole Atmosphere Community Climate Model used here was WACCM6, developed from the second iteration of the fully coupled Community Earth System Model (CESM2) (Danabasoglu et al., 2020). WACCM6 extends vertically from the Earth's surface to the lower thermosphere at ~ 140 km. For this study, we used a specific

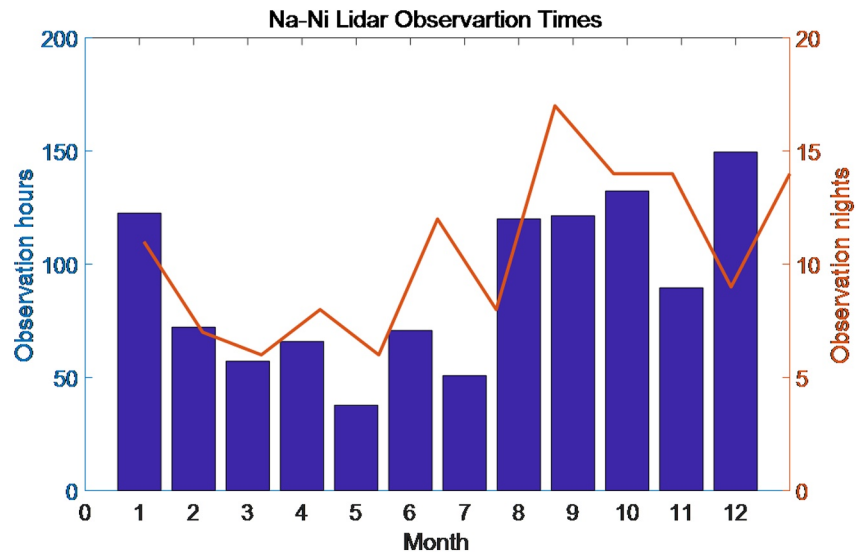


Figure 2. Statistics of the observational hours and nights of observation in each calendar month, made by the Beijing Na-Ni lidar. The measurement took place from April 2019 to March 2020 and April 2021 to August 2021.

dynamics (SD) version of WACCM6 (Plane et al., 2018), nudged with NASA's ModernEra Retrospective Analysis for Research and Applications (MERRA2) (Molod et al., 2015). The model has a horizontal resolution of 1.9° latitude \times 2.5° longitude and 88 vertical model levels (height resolution ~ 3.5 km in the MLT). The original Na chemistry in our first WACCM-Na model (Marsh et al., 2013), with some updates (Plane et al., 2015), was ported into WACCM6 for this study. The Ni MIF and its latitudinal/season variations are described in Daly et al. (2020). The Na MIF was taken from Carrillo-Sánchez et al. (2020) and treated in the same way as the Ni MIF. The model simulations were performed for a whole year following on from our earlier Ni layer modeling study (Daly et al., 2020) and now included the updated Na layer modeling work in WACCM6. Hourly output of global fields of Ni, Na, and related species was stored during the simulation.

3. Results

3.1. Seasonal Variation of the Ni and Na Layers

The observed and modeled seasonal variations of the Ni and Na layers are illustrated in Figures 3–6. Figure 3a shows the observed monthly mean Ni density as a function of height and month from the full data set consisting of 126 nights (including sporadic Ni layers). The raw Ni observations were smoothed by accumulating signal for 30 min time intervals in 2 km altitude bins. A Hamming window with a full width at half maximum of 1 km was also used to oversample the lidar data. The nightly averages of the resulting data were then used to compute the monthly mean profiles shown in Figures 3a and 4a. There is a clear annual variation in the layer with a minimum peak density in summer (May – July) of ~ 120 cm^{-3} at an 85-km altitude, when the layer is also narrower. The peak density occurs in midwinter (December – January), where the layer peak is ~ 2 km lower with a peak density of ~ 400 cm^{-3} . There is perhaps a secondary peak in autumn (October/November) with a peak density of ~ 250 cm^{-3} at 86 km. Figure 3b shows the monthly averaged Ni density as a function of height and month, simulated by WACCM-Ni. The model captures the annual variation with a midsummer minimum. However, although the peak density in winter is in good agreement with the observations (Figure 3a), the midsummer minimum value of ~ 200 cm^{-3} is not as low as that observed. Note that the model also predicts an autumnal secondary maximum though a month earlier than observed.

Inspection of Figure 3a shows that between May and July, a secondary Ni layer was observed above 95 km, which is not simulated by the model. Note that in July, an intense, narrow layer of Ni was observed at 95 km for only 2 hr (unlike the secondary layers in May and June, which were present nearly continuously). The July layer (not shown) was most likely a sporadic metal layer (Plane, 2003); since there were relatively few measurement hours during July, this has been removed from the data set in order to avoid distorting the monthly average.

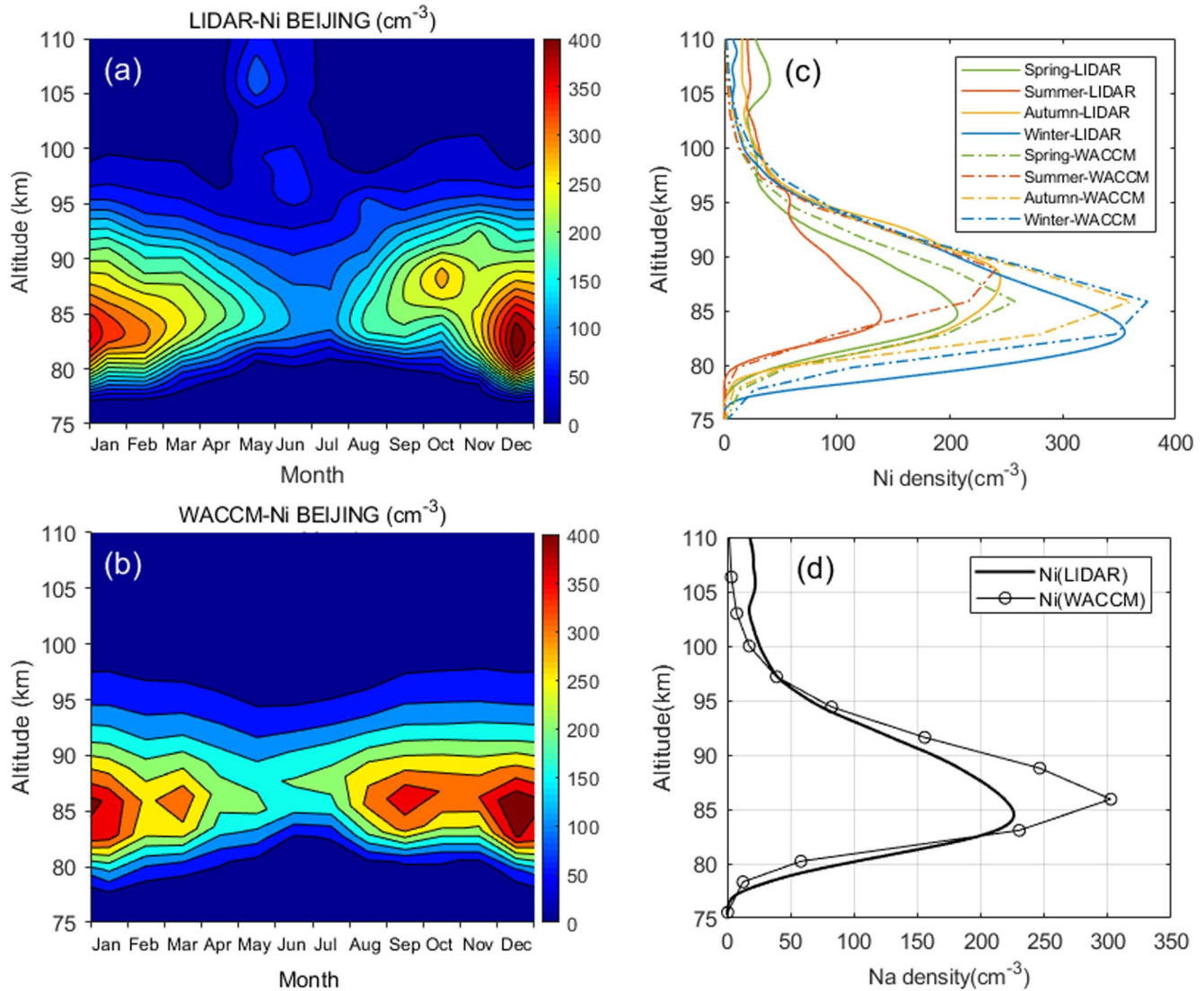


Figure 3. (a) Contour plot of the measured monthly mean Ni density as a function of month and altitude over Beijing (40°N). Note that the seasonal maximum of the Ni density occurs in December and the minimum in June. (b) Contour plot of the Ni density versus month and altitude over Beijing (40°N), simulated by the WACCM-Ni model. (c) Height profiles of the average measured and modeled Ni density in different seasons. (d) Height profile of the average Ni density for the entire lidar data set compared with WACCM-Ni. Note that all observations and model data are nighttime only.

Figure 3c shows vertical profiles of the Ni density averaged over each season. For the lidar, the average peak density in spring (green solid line) is 181 cm⁻³ at 84.8 km; in summer (red solid line), the peak density is 146 cm⁻³ at 84.6 km; in autumn (orange solid line), the peak density is 272 cm⁻³ at 87.1 km; and in winter (blue solid line), the peak density is 384 cm⁻³ at 82.6 km. That is, the layer is lower at the solstices than the equinoxes and particularly low in midwinter. In all four seasons, the Ni layer has a steeper density gradient (scale height) on the bottom side compared with the topside. This feature is captured by WACCM-Ni (dashed-dotted lines in Figure 3c), which also predicts that the layer is lowest in winter. However, although the model captures the bottom side (78–84 km) of the summertime layer well, it then greatly overpredicts the Ni density above 85 km with the peak density altitude ~5 km higher than observed.

Figure 3d compares the observed and modeled annual average nighttime Ni layer. The WACCM-Ni peak density is 311 cm⁻³ at 85.9 km, which is 41% larger than the observed average peak density of 221 cm⁻³ at 84.8 km.

Figures 4a and 4b show the monthly mean Na density as a function of height and month, measured by lidar and modeled by WACCM-Na, respectively. The observed layer exhibits an annual cycle with a maximum in

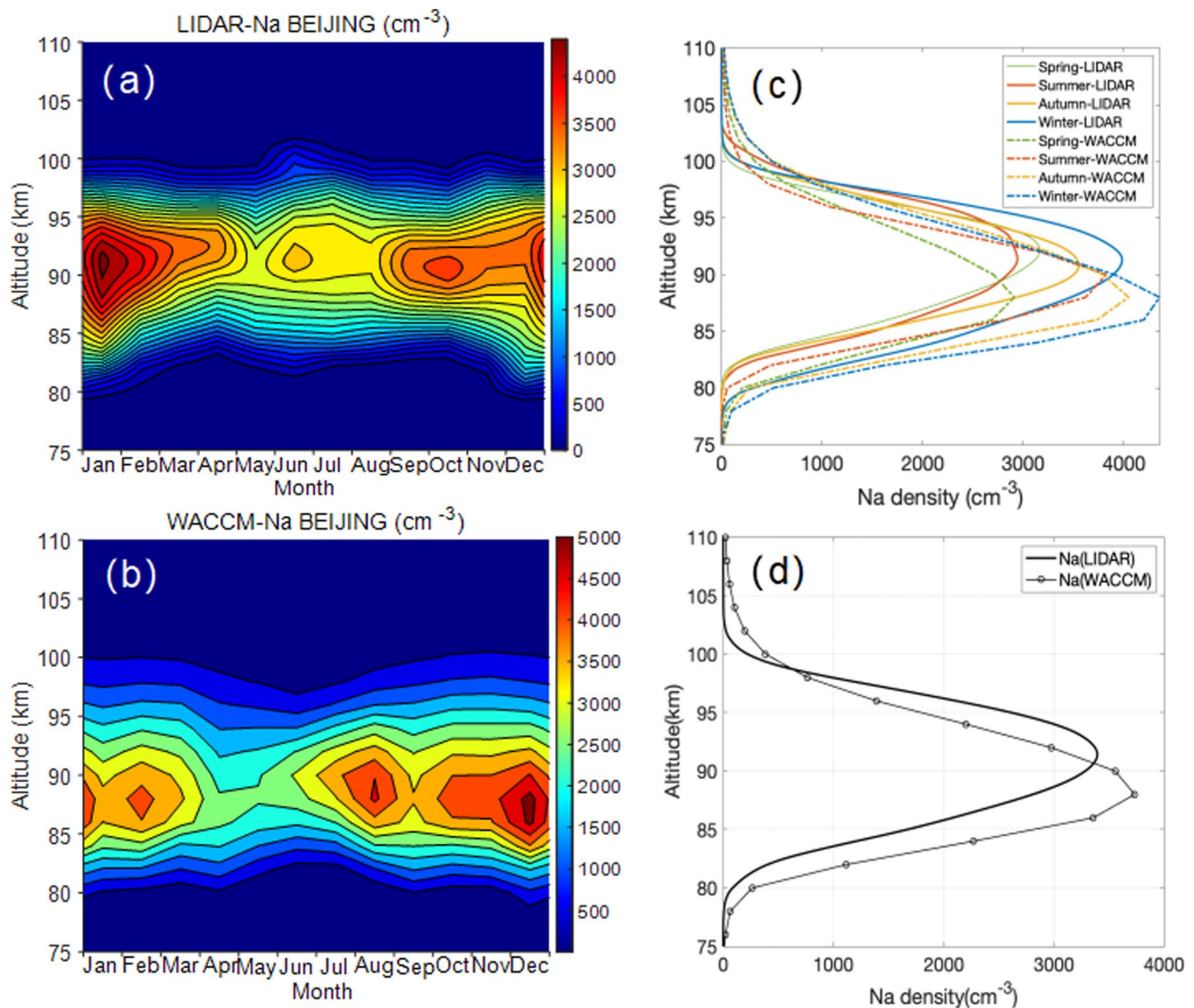


Figure 4. (a) Contour plot of the measured monthly mean Na density as a function of month and altitude over Beijing (40°N). (b) Contour plot of the Na density versus month and altitude over Beijing (40°N), simulated by the WACCM-Na model. (c) Height profiles of the average measured and modeled Na density in different seasons. (d) Height profile of the average Na density for the entire lidar data set compared with WACCM-Na. Note that all observations and model simulations are for nighttime only.

midwinter that is ~ 3 times higher than the minimum in early summer (May); these features are satisfactorily captured by WACCM-Na. Both observations and the model also suggest a secondary maximum later in the year in August (WACCM-Na) or October (lidar). Figure 4c shows the average Na layer in each season. The modeled layer peak is consistently 3–4.5 km below the observed peak and has a higher peak density apart from in spring. These discrepancies are summarized in Figure 4d, which compares the annual average observed and modeled layers.

In order to compare further the observed and modeled seasonal variations of the Ni and Na layers, we now examine the seasonal variations of their column abundances, peak densities, centroid heights, and RMS widths. The results are shown in Figure 5 for Ni and Figure 6 for Na; the blue lines are the monthly mean values observed by lidar, and the red curves are the corresponding modeled values. Figure 5a shows the annual variation in Ni peak density with a midwinter peak and a midsummer maximum, which the model captures well in the first 6 months but then overestimates between July and November. Figure 5b demonstrates that the Ni column abundance varies

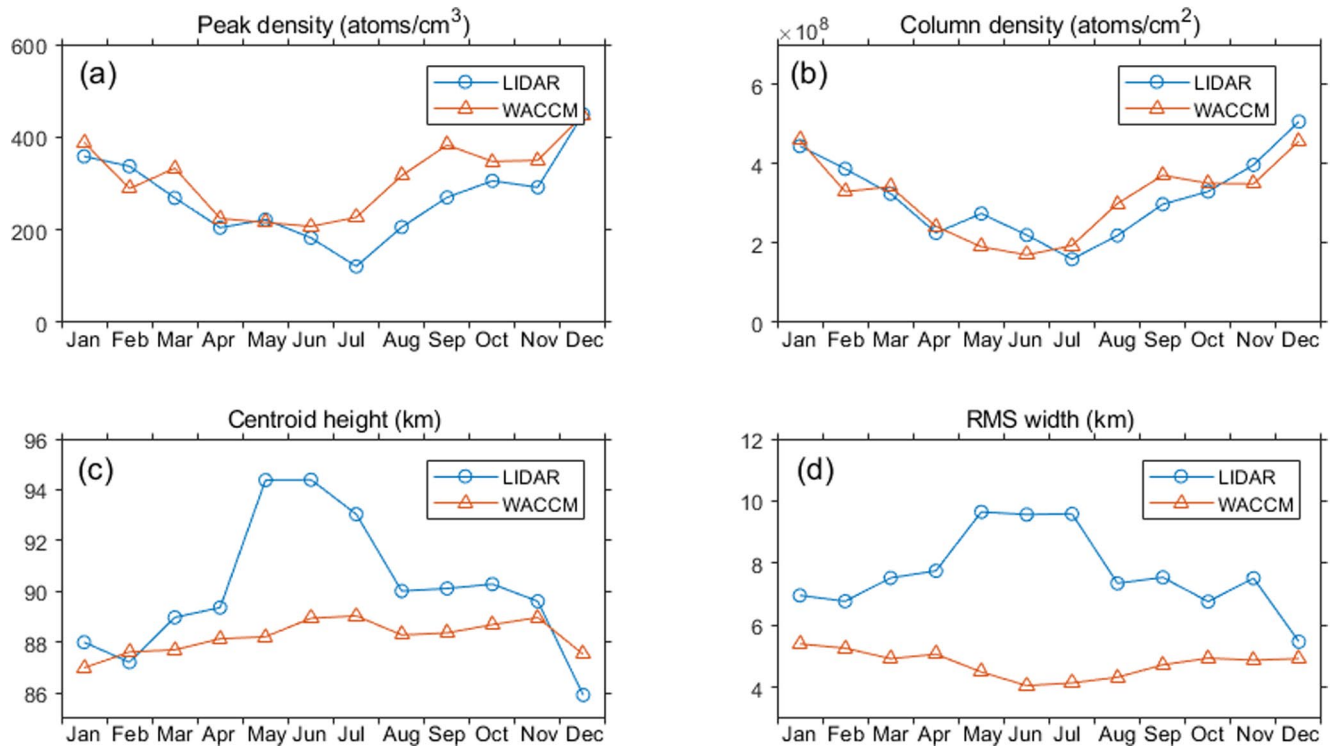


Figure 5. Comparison of the nighttime monthly Ni layer parameters at Beijing measured by lidar (blue lines) and modeled by WACCM-Ni (brown lines): (a) peak density, (b) column abundance, (c) centroid height, and (d) RMS width between 70 and 120 km.

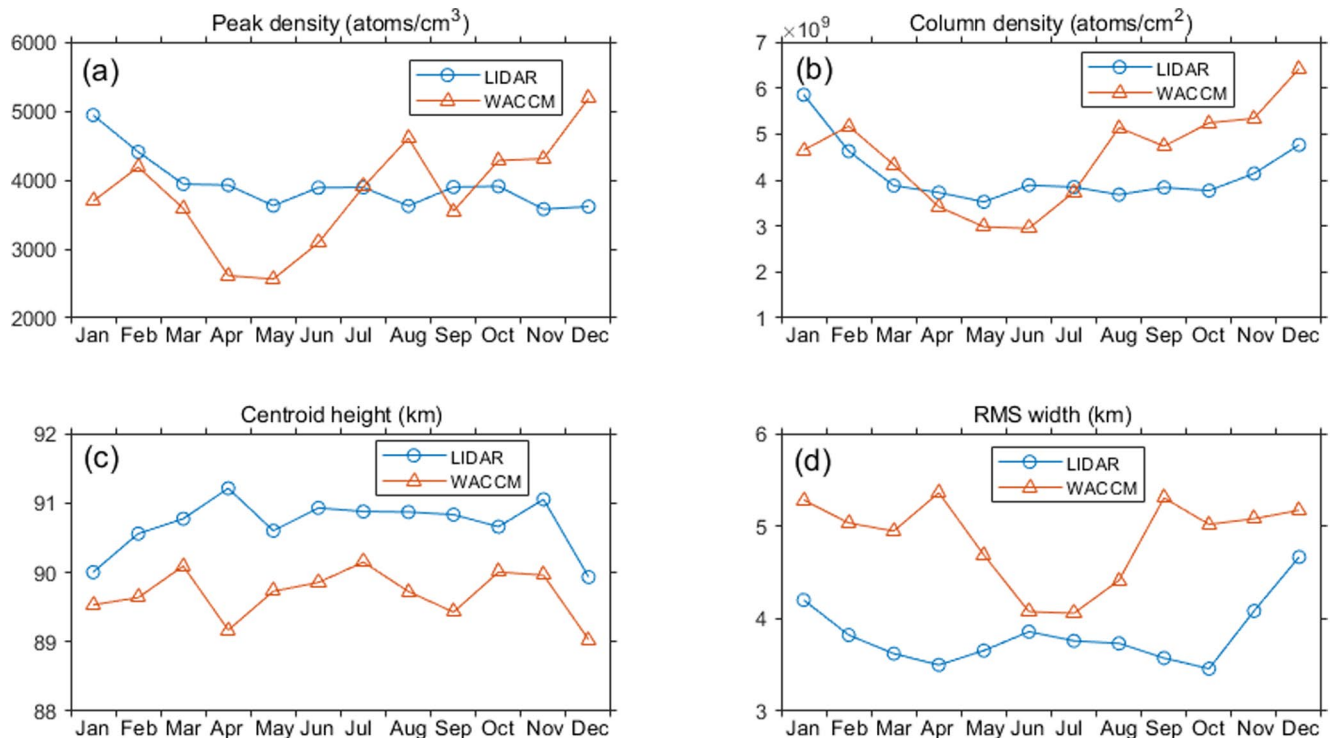


Figure 6. Comparison of the nighttime monthly Na layer parameters at Beijing measured by lidar (blue lines) and modeled by WACCM-Ni (brown lines): (a) peak density, (b) column abundance, (c) centroid height, and (d) RMS width between 70 and 120 km.

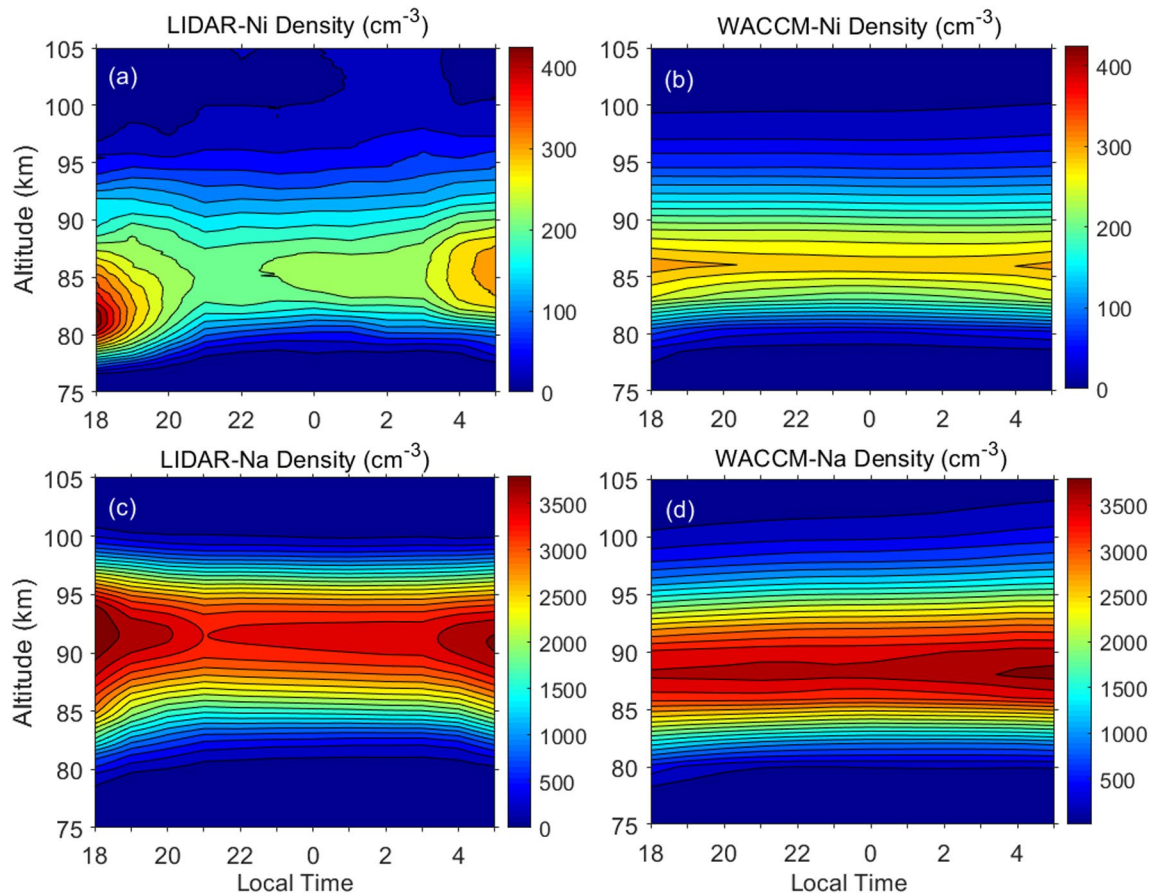


Figure 7. Comparison of the observed and modeled seasonally averaged nocturnal variations of the Ni and Na density versus height: (a) Lidar-Ni, (b) WACCM-Ni, (c) Lidar-Na, and (d) WACCM-Na.

from a midsummer minimum of 1.8×10^8 to a midwinter maximum of $5.7 \times 10^8 \text{ cm}^{-2}$ with an annual mean of $3.3 \times 10^8 \text{ cm}^{-2}$. This behavior is captured very well by WACCM-Ni over the entire year.

The monthly variation of the centroid height is shown in Figure 5c. Ignoring the measured centroid height in May – July, which is distorted by the high-lying secondary layers (see Figure 3a), there is good agreement with the model prediction of a small increase in the layer height of 1–2 km during summer. The monthly variation of the Ni layer RMS width is plotted in Figure 5d. Again, ignoring the observations between May and July, both observations and model indicate little seasonal variation (<1.5 km) in the layer width though the modeled layer is consistently narrower.

In the case of the Na layer, Figure 6a shows there is more variability in the modeled peak density than that observed. In contrast, the agreement in the annual variation of the Na column density (Figure 6b) is much better: the measured column abundance has a minimum in May of $3.5 \times 10^9 \text{ cm}^{-2}$ and a maximum in January of $5.8 \times 10^9 \text{ cm}^{-2}$, whereas the model minimum is $2.8 \times 10^9 \text{ cm}^{-2}$ in June and the maximum is $6.4 \times 10^9 \text{ cm}^{-2}$ in December. Figure 6c shows that the measured and modeled centroid height have very similar seasonal variations though the modeled layer is on average ~ 1 km lower. Note that the Ni layer centroid height is observed to be around 2 km lower than the Na layer in agreement with the model. Figure 6d shows the monthly RMS width of the Na layer. Apart from midsummer, WACCM-Na predicts a layer that is ~ 1.5 km wider than that observed.

3.2. Nocturnal Variation of the Ni and Na Layers

Figure 7 compares the observed and modeled annual average nighttime variation of the Ni and Na layers as a function of altitude and local solar time (18:00–05:00 LT). The monthly averages of the observed nighttime

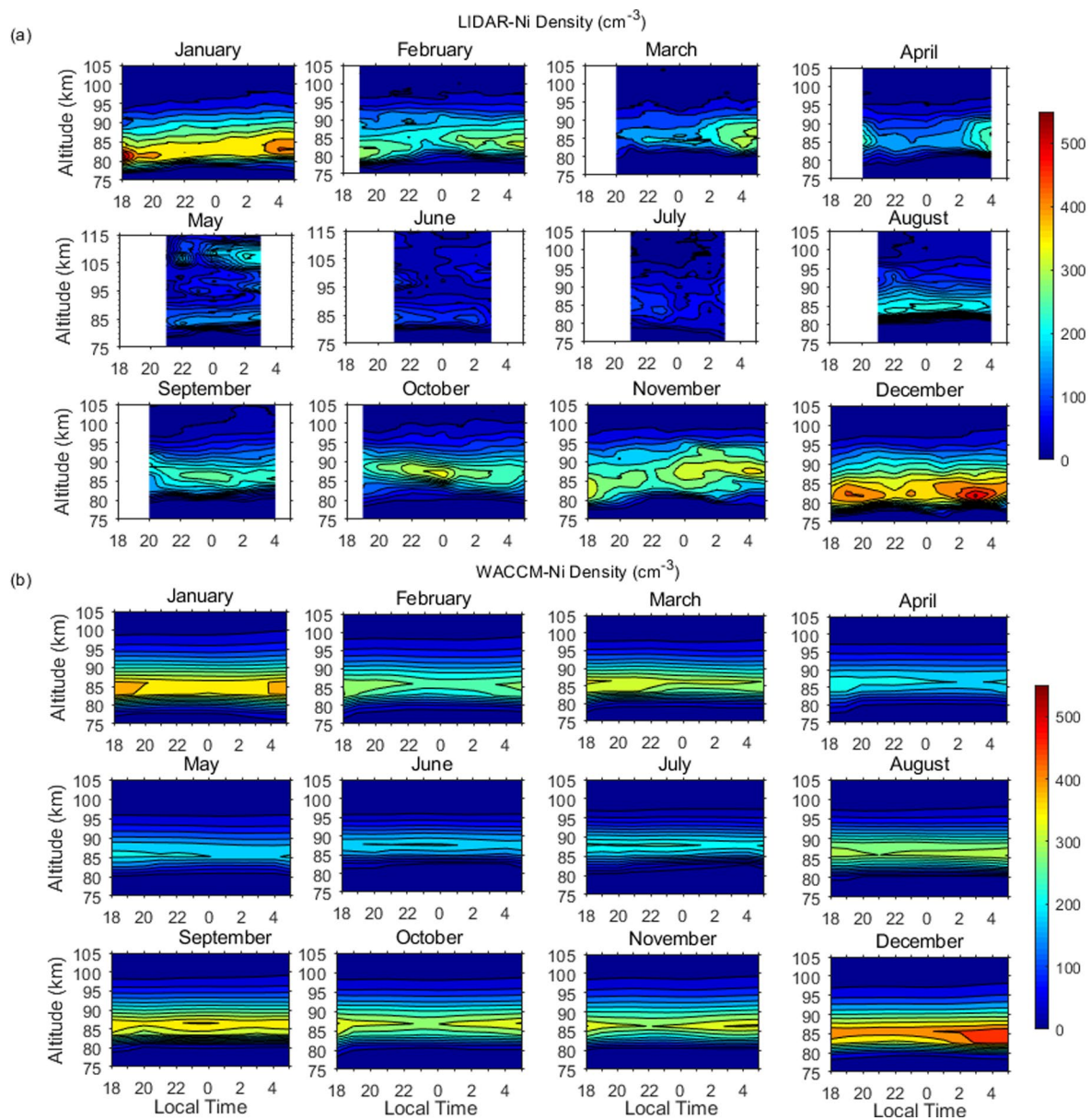


Figure 8. Comparison of the observed and modeled nocturnal variations of the Ni density (atom cm^{-3}) for each month of the year: (a) Lidar-Ni and (b) WACCM-Ni. Note that the plots for May and June in panel (a) are extended to a height of 115 km in order to show the high-lying Ni layers that were observed during these summer months.

variation are illustrated in Figure 8a for Ni and Figure 9a for Na. These plots show that in the summer months, there is no data before 21:00 LT or after 03:00 LT and before 20:00 or after 04:00 during spring and autumn. This means that the annual average data in Figure 7 are strongly biased to the winter months before 20:00 and after 04:00 LT. Since the wintertime layers have higher concentrations (Figures 3 and 4), this largely explains the apparent increase in both metals at the start and end of the night. Nevertheless, inspection of Figure 8a shows that in January and December there are increases in the observed peak density in the early evening (<21:00 LT) and early morning (>02:00 LT) and some evidence of this behavior in February, April, and November. This nocturnal variability is also seen in some months (January, February, April, October, and November) in the WACCM-Ni simulations in Figure 8b. During the period from 21:00 to 02:00 LT, where the annual average in Figure 7 represents contributions from most of the year, there is very little variation in the Ni layer, and this behavior is well-simulated by WACCM-Ni. The model also satisfactorily predicts the layer peak height in the individual months.

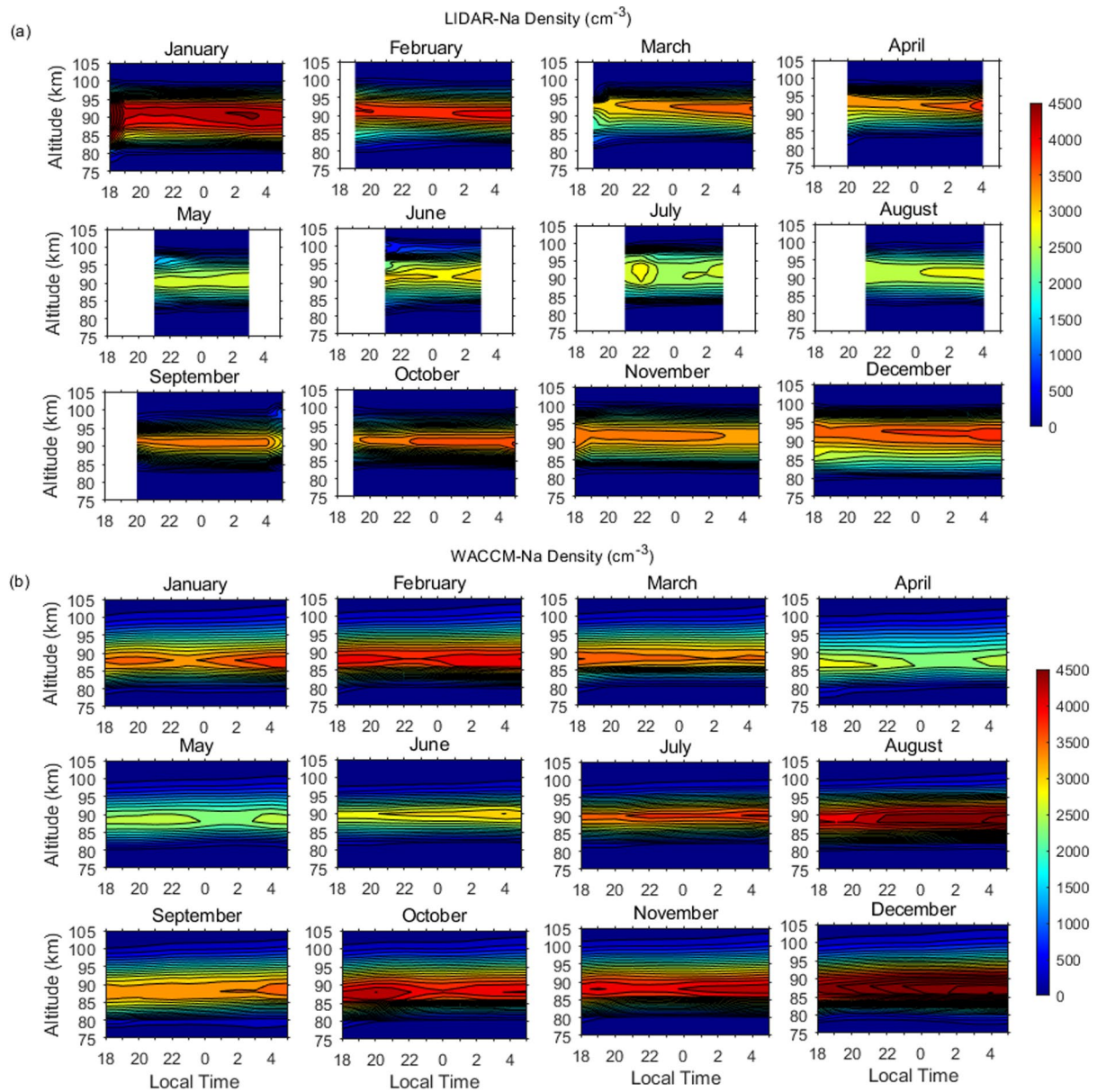


Figure 9. Comparison of the observed and modeled nocturnal variations of the Na density (atom cm⁻³) for each month of the year: (a) Lidar-Na and (b) WACCM-Na.

Although the observed annual average Na layer does exhibit early evening and early morning maxima (Figure 7), the comparison with the individual months in Figure 9a shows that this arises from the winter bias in the average before 20:00 and after 04:00, because this variation is essentially absent in the individual winter months. Although this nocturnal behavior is satisfactorily simulated by WACCM-Na in Figure 9b, the modeled Na layer peak is 3–4 km too low in all months.

One feature in Figure 8a is the presence of high-lying secondary Ni layers during the summer months May and June. Although this was the period with the least observation nights (see Figure 2), these secondary layers were present on nearly every night during these months and so are clearly visible in the monthly average layer profile plotted in Figure 3. Particularly striking is the absence of any corresponding layers in the Na observations in Figure 9a.

4. Discussion

4.1. Comparison With Other Observations

The nightly mean Ni peak density at Beijing (40°N, 116°E) is between ~ 150 and 500 cm^{-3} with a column abundance ranging from 1.5×10^8 to $4.5 \times 10^8 \text{ cm}^{-2}$. These measurements are in good accordance with the previous measurements at K hlungsborn, Germany (54°N, 12°E), where the nightly mean Ni peak density from a limited set of measurements between January and March was between ~ 280 and 450 cm^{-3} and the column abundance between 3.1×10^8 and $4.9 \times 10^8 \text{ cm}^{-2}$ (Gerding et al., 2019). Clearly, the ~ 50 times higher Ni column abundance measured at Chatanika, Alaska (65°N, 147°W) (Collins et al., 2015) is anomalous, as discussed by Gerding et al. (2019).

The present study reports the full seasonal variation of the Ni layer for the first time. The layer exhibits a pronounced annual variation at this midlatitude location, increasing by a factor of ~ 3 from a summertime minimum to a midwinter peak (Figures 3 and 5). This seasonal behavior is similar to that of the midlatitude Na layer (Figures 4 and 6) and the Fe layer (Plane, 2003; Yi et al., 2009). The seasonal variations of the Na and Fe layers increase with latitude from almost no variation at the equator to a factor of ~ 9 at the poles (Feng et al., 2013; Gardner et al., 2005; Marsh et al., 2013), similar to the seasonal variation of Ni predicted by WACCM-Ni (Daly et al., 2020).

The annual mean column densities of Ni and Na from the present study are 3.1×10^8 and $2.5 \times 10^9 \text{ cm}^{-2}$, respectively, and that of Fe is $7.5 \times 10^9 \text{ cm}^{-2}$ (Yi et al., 2009), giving a mean Na:Ni ratio of 8.1 and a mean Fe:Ni ratio of 24.2. The ratio of the meteoric input functions for these pairs of metals predicted by the CABMOD-ZoDy coupled models is 3.8 for Na:Ni and 16.3 for Fe:Ni (Carrillo-S nchez et al., 2020) compared with their respective CI ratios of 1.2 and 17.8 (Asplund et al., 2009). The atmospheric Fe:Ni ratio is therefore close to the modeled injection rates and the CI ratio of the two metals (and lower than the ratio of 38:1 reported by Gerding et al. (2019) from a small set of measurements). The atmospheric ratio is also very close to a $\text{Fe}^+:\text{Ni}^+$ ratio of 29.0 measured during five rocket flights (Kopp, 1997).

The Na:Ni ablation ratio predicted by CABMOD-ZoDy is ~ 3 times larger than the CI ratio of these metals because Na ablates much more efficiently than the more refractory Ni from molten cosmic dust particles (Bones et al., 2019). The measured Na:Ni ratio is then ~ 2 times larger than the ablation ratio. This is largely explained by the more efficient neutralization of Na^+ ions between 90 and 100 km (see below), consistent with a $\text{Na}^+:\text{Ni}^+$ ratio of only 2.2 (i.e., 60% of the ablation ratio) measured by rocket-borne mass spectrometry (Kopp, 1997).

It is worth noting that the seasonal variation of Ni, Na, and Fe is quite different from the semi-annual seasonal variations of the Ca and K layers at mid-latitudes, which exhibit maxima in summer and winter, and minima in spring and autumn. The column abundance of the Ca layer measured at midlatitudes (K hlungsborn, 54°N) is $2.1 \times 10^7 \text{ cm}^{-2}$ (Plane et al., 2018), which is smaller than the Ni column abundance by a factor of 14.8, despite the CI abundance of Ca being 1.2 times larger than that of Ni (Asplund et al., 2009). This reflects the very refractory nature of Ca in a silicate melt (Carrillo-S nchez et al., 2020). The column abundance of the K layer measured at midlatitudes (Beijing, 40°N) is $1.0 \times 10^8 \text{ cm}^{-2}$ (Wang et al., 2017). This is a factor of 3.1 times smaller than the Ni abundance, whereas the CI abundance of K is 13 times smaller than that of Ni (Asplund et al., 2009). So, this represents the contrasting situation where the relatively volatile K ablates very efficiently during atmospheric entry (Carrillo-S nchez et al., 2020).

4.2. Contrasting Behavior of Ni and Na

Figures 10a and 10b illustrate the observed and modeled seasonal variations of the Na:Ni density ratio as a function of altitude. Both plots show that the maximum of the ratio occurs around 95 km irrespective of season. The modeled maximum value is ~ 30 . Although this agrees well with the observed ratio in autumn and early winter (September – November), larger values are measured during the rest of the year, reaching ~ 80 during April – August. The main reason for this discrepancy is that the modeled Na layer is ~ 3 km lower than that observed (Figure 4), whereas WACCM-Ni simulates the correct peak height of the Ni layer (Figure 3). This suggests that further development of the Na chemistry in WACCM-Na may be needed, but that is beyond the scope of this paper, which focuses on the Ni layer.

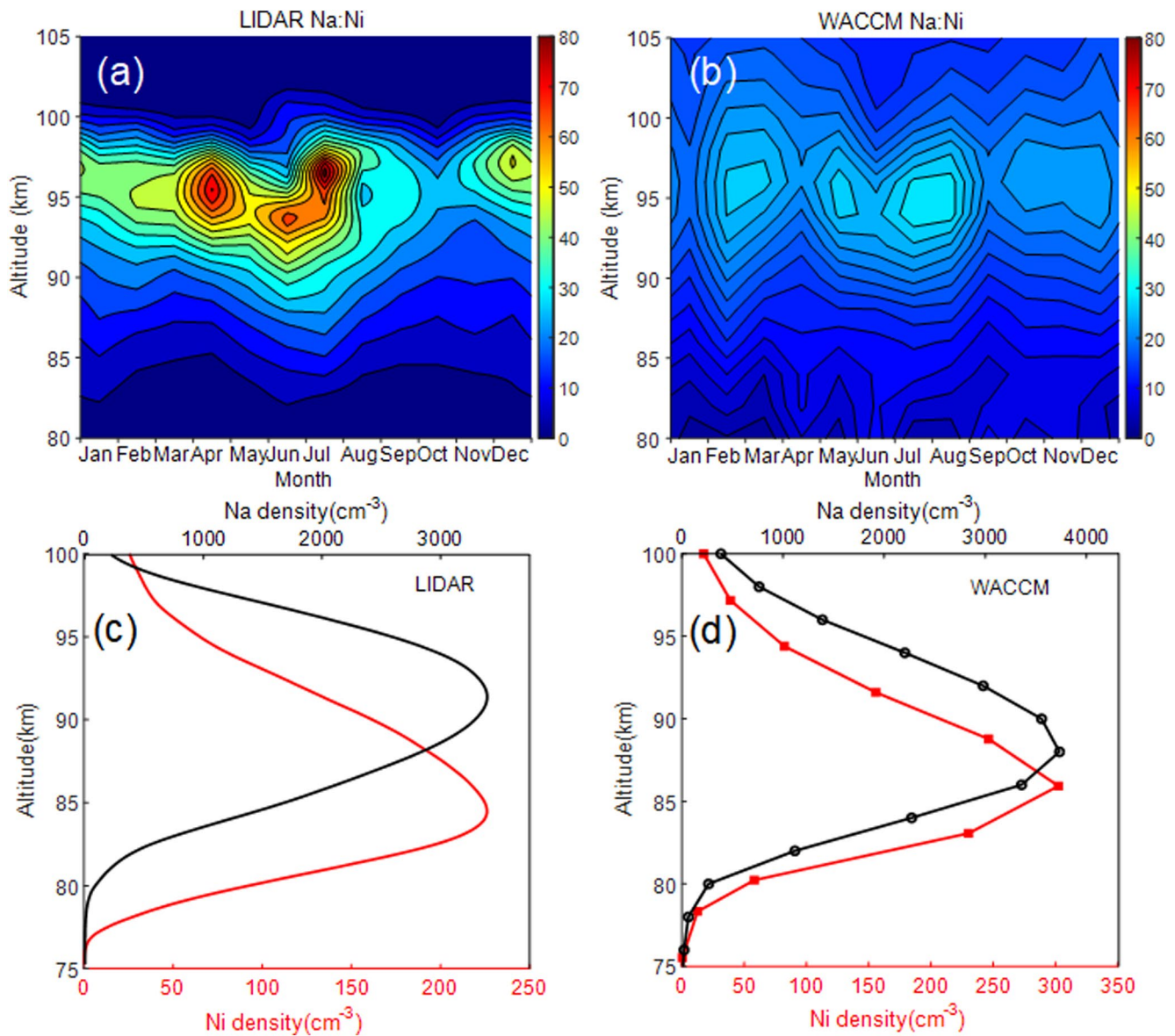
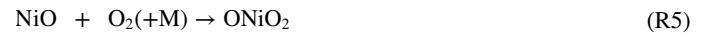


Figure 10. Height profiles of the monthly averaged ratio of the Na and Ni nighttime densities at Beijing as a function of month: (a) observed by lidar and (b) modeled by WACCM. The height profiles of the annual average Ni and Na densities are shown in (c) for the observations and in (d) for the model.

Figures 10c and 10d compare the observed and modeled annual night-time average profiles of the Ni and Na layers at 40°N. The observed bottom-side of the Ni layer (76–83 km) is 3–5 km lower than the bottom-side of the Na layer (79–88 km), and the peak of the Ni layer is 8 km lower. This relative downward displacement of the Ni layer is also captured by WACCM (Figure 10d), though the displacement is smaller because the modeled Na layer is too low.

We now examine the differences between the chemistries of Ni and Na, which affect the bottom side and topsides of their respective layers. In the case of Ni, oxidation by O_3 to form NiO is followed either by recycling to Ni by O, CO, or O_3 or by oxidation to higher oxides (NiO_2 and $ONiO_2$):





where M is a third body (N_2 or O_2) (Daly et al., 2020; Mangan et al., 2019). However, the higher oxides are only temporary reservoirs because atomic O can efficiently reduce them back to NiO and then to Ni via R2 or R3 (Daly et al., 2020):



The situation for Na is rather different. Na is also oxidized by O_3 , and NaO can be reduced back to Na by O. However, NaO reacts very rapidly with H_2O to form NaOH, which then recombines rapidly with CO_2 to make NaHCO_3 (Plane, 2004):



Both NaOH and NaHCO_3 can be reduced back to Na by atomic H:



However, although R12 is a fast reaction with a large rate coefficient (Gómez-Martín et al., 2017), the concentration of H is about 3 orders of magnitude lower than O (Plane et al., 2015). Furthermore, R13 is relatively slow because it has a significant activation energy (Cox et al., 2001), so that NaHCO_3 is a stable reservoir for Na below 87 km. This explains the large depletion of Na compared with Ni below this altitude (Figure 10c).

Two previous lidar studies of the Ni layer (Collins et al., 2015; Gerding et al., 2019) reported that the layer bottom side is 1–2 km lower than the Fe layer between 78 and 85 km. Our subsequent modeling study (Daly et al., 2020) showed that this was due to the relatively fast reaction between NiO and CO (reaction R3), which takes over from reaction with atomic O (reaction R2) below 83 km in recycling NiO back to Ni. This extension of the Ni layer to below 80 km results in the unusually large RMS width of the layer: Figure 6 shows that the average width is ~7 km (excluding the summer months with high-lying secondary Ni layers) compared with ~4 km for the Na layer (Figure 7).

The topsides of the metal layers are controlled by ion-molecule chemistry. Charge transfer of the metal atoms with the ambient lower *E* region ions NO^+ and O_2^+ is the main pathway by which metal atoms are ionized, and the reactions of different metal atoms tend to have similar rate coefficients since these reactions proceed close to their Langevin collision frequency limits (Plane et al., 2015). It is therefore the chemistry that neutralizes the metal ions, which is largely responsible for the different metal atoms/ion ratios. In the case of Ni^+ , oxidation by O_3 forms NiO^+ , which can then undergo dissociative recombination with an electron to yield Ni. However, NiO^+ also reacts rapidly with atomic O and so is overwhelmingly reduced back to Ni^+ , given the relative concentration of O and electrons in the lower *E* region (Bones et al., 2020):



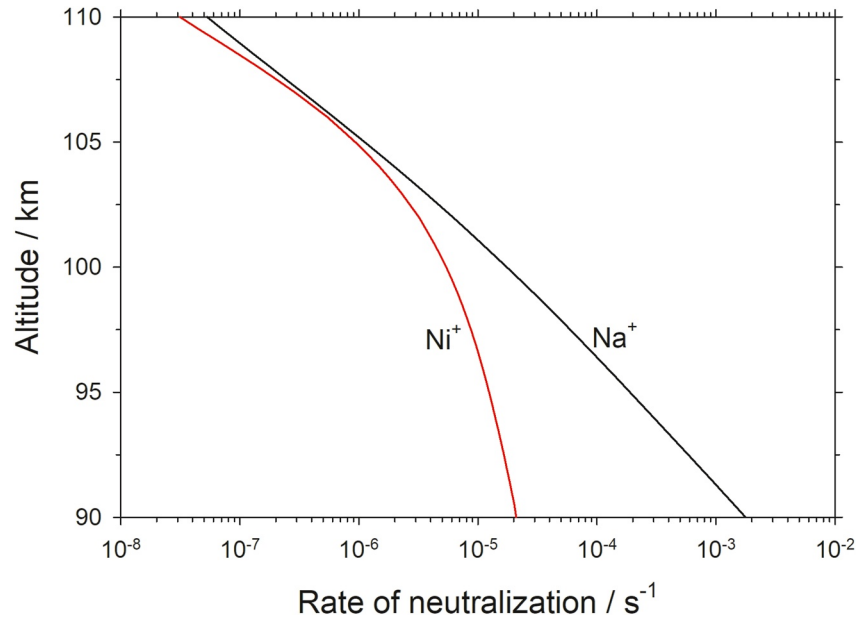


Figure 11. First-order rate of neutralization of Ni⁺ and Na⁺ ions as a function of altitude. Conditions: 40°N, April, midnight.

Na⁺ ions cannot react with O₃ because the NaO⁺ bond is too weak (Cox & Plane, 1998). Instead, Na⁺ recombines with N₂, and the resulting Na⁺.N₂ cluster ion either switches with CO₂ to make a stable cluster ion which will recombine with an electron, or undergoes a slow reaction with O which usually leads back to Na⁺ (Cox & Plane, 1998; Plane, 2004):

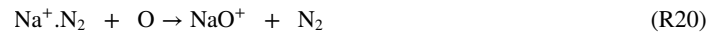
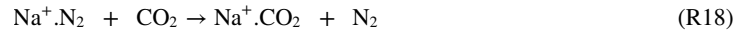


Figure 11 illustrates the first-order neutralization rates of Ni⁺ and Na⁺ as a function of height, calculated using rate coefficients for R14 – R16 from Bones et al. (2020) and R17 – R20 from Plane et al. (2015). This shows that Na⁺ is neutralized much more rapidly than Ni⁺ below 100 km, which explains why the topside of the Na layer only starts above 92 km compared with 84 km for the Ni layer (Figure 10a).

The presence of a relatively large fraction of Ni⁺ relative to Ni between 90 and 105 km, compared with Na⁺ to Na, probably also explains the high-lying Ni layers observed during the summer months (Figure 8), which were not seen simultaneously for Na (Figure 9). The lifetime of Ni⁺ under average conditions is a day or even longer above 95 km (Figure 11). This means that if dynamical forcing (e.g., tides, waves, or wind shears) concentrates the relatively long-lived Ni⁺ as well as the dominant Fe⁺ and Mg⁺ ions (Plane et al., 2015) into a layer, then the corresponding layer of enhanced electron density will result in fast neutralization of Ni⁺ via reaction R15. The resulting Ni layer will also stand out against the relatively depleted neutral Ni atoms above 90 km, in contrast to Na.

The modeled annual variations of both the Ni and Na layers are simulated satisfactorily (Figures 3, 4, 5 and 6). In the case of Ni, the summertime minimum largely arises from the reaction between ONiO₂ and O (R6), which has a significant activation energy of 19.2 kJ mol⁻¹ (Daly et al., 2020). This reaction therefore becomes very slow at the low temperatures that characterize the summertime MLT, so that ONiO₂ becomes a more effective reservoir species. That said, ONiO₂ also reacts with H to form NiOH, which can then react with H to reform Ni (Daly et al., 2020), thereby reducing the effectiveness of ONiO₂ as a reservoir (and ameliorating the effect of the

temperature dependence of R6). For Na, the reaction of NaHCO_3 with H (R13) also has a significant activation energy of 9.9 kJ mol^{-1} , which is largely responsible for the seasonal variation of the layer (Cox et al., 2001).

5. Conclusions

This study is the first investigation of the Ni layer in the midlatitude MLT over a full seasonal cycle. An interesting contrast in the morphology, nocturnal variation, and seasonal behavior of the layer was provided by simultaneous observations of the very well-studied Na layer. A total of 126 nights (1090 hr) of Ni/Na lidar data were used and compared to simulations from the whole atmosphere chemistry-climate model WACCM.

The observations reveal that the Ni layer has a strong seasonal cycle with a maximum in winter and minimum in summer, closely following the seasonal cycle of the Na layer. The Ni layer peak occurs about 8 km below that of Na, so that most of the Ni atom abundances are located below 90 km, whereas most of the Na abundances occur above 90 km. These features are captured satisfactorily by the WACCM-Ni and WACCM-Na model simulations (although the modeled Na layer peak is ~ 3 km lower than observed) and are explained by significant differences in the neutral chemistry of Ni and Na below 90 km and their ion-molecule chemistry between 90 and 100 km. One striking feature is the common occurrence during summer of secondary Ni layers above 90 km, which was not observed in the case of Na. Future studies of this phenomenon would benefit from simultaneous lidar measurements of temperature, wind, and Ca^+ ions to explore the ion-neutral coupling, which is most likely involved.

Data Availability Statement

The lidar data and model output used in the paper are archived and available at <https://doi.org/10.5281/zenodo.5729789>.

Acknowledgments

This work was supported by: the Youth Innovation Promotion Association of CAS (Grant No. 2019150); the Pandeng Program of the National Space Science Center, Chinese Academy of Sciences; the Natural Science Foundation of China (Grant No. 41627804); the NNSC research fund for key development directions; the Specialized Research Fund for State Key Laboratories of China; the International Partnership Program of the Chinese Academy of Sciences (Grant No. 183311KYSB20200003); the Chinese Meridian Project; the China-Brazil Joint Laboratory for Space Weather; and the UK Natural Environment Research Council Grant (Grant No. NE/P001815/1).

References

- Asplund, M., Grevesse, N., Sauval, A. J., & Scott, P. (2009). The chemical composition of the sun. *Annual Review of Astronomy and Astrophysics*, 47, 481–522. <https://doi.org/10.1146/annurev.astro.46.060407.145222>
- Bones, D. L., Carrillo-Sánchez, J. D., Kulak, A. N., & Plane, J. M. C. (2019). Ablation of Ni from micrometeoroids in the upper atmosphere: Experimental and computer simulations and implications for Fe ablation. *Planetary and Space Science*, 179, 104725. <https://doi.org/10.1016/j.pss.2019.104725>
- Bones, D. L., Daly, S., Mangan, T. P., & Plane, J. M. C. (2020). A study of the reactions of Ni^+ and NiO^+ ions relevant to planetary upper atmospheres. *Physical Chemistry Chemical Physics*, 22, 8940–8951. <https://doi.org/10.1039/D0CP01124J>
- Carrillo-Sánchez, J. D., Gómez-Martín, J. C., Bones, D. L., Nesvorný, D., Pokorný, P., Benna, M., et al. (2020). Cosmic dust fluxes in the atmospheres of Earth, Mars, and Venus. *Icarus*, 335, 113395. <https://doi.org/10.1016/j.icarus.2019.113395>
- Chu, X., & Papen, G. (2005). Resonance fluorescence lidar for measurements of the middle and upper atmosphere. In T. Fujii, & T. Fukuchi (Eds.), *Laser remote sensing* (pp. 179–432). CRC Press. <https://doi.org/10.1201/9781420030754.ch5>
- Collins, R. L., Li, J., & Martus, C. M. (2015). First lidar observation of the mesospheric nickel layer. *Geophysical Research Letters*, 42, 665–671. <https://doi.org/10.1002/2014gl062716>
- Cox, R. M., & Plane, J. M. C. (1998). An ion-molecule mechanism for the formation of neutral sporadic Na layers. *Journal of Geophysical Research*, 103, 6349–6359. <https://doi.org/10.1029/97JD03376>
- Cox, R. M., Self, D. E., & Plane, J. M. C. (2001). A study of the reaction between NaHCO_3 and H: Apparent closure on the chemistry of mesospheric Na. *Journal of Geophysical Research: Atmospheres*, 106, 1733–1739. <https://doi.org/10.1029/2000JD900579>
- Daly, S. M., Feng, W., Mangan, T. P., Gerding, M., & Plane, J. M. C. (2020). The meteoric Ni layer in the upper atmosphere. *Journal of Geophysical Research: Space Physics*, 125, e2020JA028083. <https://doi.org/10.1029/2020JA028083>
- Danabasoglu, G., Lamarque, J.-F., Bacmeister, J., Bailey, D. A., DuVivier, A. K., Edwards, J., et al. (2020). The community Earth system model version 2 (CESM2). *Journal of Advances in Modeling Earth Systems*, 12, e2019MS001916. <https://doi.org/10.1029/2019MS001916>
- Dunker, T., Hoppe, U.-P., Feng, W., Plane, J. M. C., & Marsh, D. R. (2015). Mesospheric temperatures and sodium properties measured with the ALOMAR Na lidar compared with WACCM. *Journal of Atmospheric and Solar-Terrestrial Physics*, 127, 111–119. <https://doi.org/10.1016/j.jastp.2015.01.003>
- Fan, Z. Y., Plane, J. M. C., Gumbel, J., Stegman, J., & Llewellyn, E. J. (2007). Satellite measurements of the global mesospheric sodium layer. *Atmospheric Chemistry and Physics*, 7, 4107–4115. <https://doi.org/10.5194/acp-7-4107-2007>
- Feng, W., Kaifler, B., Marsh, D. R., Höffner, J., Hoppe, U.-P., Williams, B. P., & Plane, J. M. C. (2017). Impacts of a sudden stratospheric warming on the mesospheric metal layers. *Journal of Atmospheric and Solar-Terrestrial Physics*, 162, 162–171. <https://doi.org/10.1016/j.jastp.2017.02.004>
- Feng, W., Marsh, D. R., Chipperfield, M. P., Janches, D., Höffner, J., Yi, F., & Plane, J. M. C. (2013). A global atmospheric model of meteoric iron. *Journal of Geophysical Research: Atmospheres*, 118, 9456–9474. <https://doi.org/10.1002/jgrd.50708>
- Fussen, D., Vanhellemont, F., Tetard, C., Matshvili, N., Dekemper, E., Loodts, N., et al. (2010). A global climatology of the mesospheric sodium layer from GOMOS data during the 2002–2008 period. *Atmospheric Chemistry and Physics*, 10, 9225–9236. <https://doi.org/10.5194/acp-10-9225-2010>
- Gardner, C. S., Plane, J. M. C., Pan, W., Vondrak, T., Murray, B. J., & Chu, X. (2005). Seasonal variations of the Na and Fe layers at the South Pole and their implications for the chemistry and general circulation of the polar mesosphere. *Journal of Geophysical Research*, 110, D10302. <https://doi.org/10.1029/2004JD005670>

- Gerding, M., Daly, S., & Plane, J. M. C. (2019). Lidar soundings of the mesospheric nickel layer using Ni(³F) and Ni(³D) transitions. *Geophysical Research Letters*, *46*, 408–415. <https://doi.org/10.1029/2018gl080701>
- Gómez-Martín, J. C., Seaton, C., de Miranda, M. P., & Plane, J. M. C. (2017). The reaction between sodium hydroxide and atomic hydrogen in atmospheric and flame chemistry. *The Journal of Physical Chemistry A*, *121*, 7667–7674. <https://doi.org/10.1021/acs.jpca.7b07808>
- Jiao, J., Yang, G., Wang, J., Cheng, X., Li, F., Yang, Y., et al. (2015). First report of sporadic K layers and comparison with sporadic Na layers at Beijing, China (40.6°N, 116.2°E). *Journal of Geophysical Research: Space Physics*, *120*, 5214–5225. <https://doi.org/10.1002/2014ja020955>
- Kopp, E. (1997). On the abundance of metal ions in the lower ionosphere. *Journal of Geophysical Research*, *102*, 9667–9674. <https://doi.org/10.1029/97JA00384>
- Langowski, M. P., von Savigny, C., Burrows, J. P., Fussen, D., Dawkins, E. C. M., Feng, W., et al. (2017). Comparison of global datasets of sodium densities in the mesosphere and lower thermosphere from GOMOS, SCIAMACHY and OSIRIS measurements and WACCM model simulations from 2008 to 2012. *Atmospheric Measurement Techniques*, *10*, 2989–3006. <https://doi.org/10.5194/amt-10-2989-20172017>
- Li, T., Ban, C., Fang, X., Li, J., Wu, Z., Feng, W., et al. (2018). Climatology of mesopause region nocturnal temperature, zonal wind and sodium density observed by sodium lidar over Hefei, China (32°N, 117°E). *Atmospheric Chemistry and Physics*, *18*, 11683–11695. <https://doi.org/10.5194/acp-18-11683-2018>
- Mangan, T. P., McAdam, N., Daly, S. M., & Plane, J. M. C. (2019). Kinetic study of Ni and NiO reactions pertinent to the Earth's upper atmosphere. *The Journal of Physical Chemistry A*, *123*, 601–610. <https://doi.org/10.1021/acs.jpca.8b11382>
- Marsh, D. R., Janches, D., Feng, W., & Plane, J. M. C. (2013). A global model of meteoric sodium. *Journal of Geophysical Research: Atmospheres*, *118*(11), 11442–11452. <https://doi.org/10.1002/jgrd.50870>
- Megie, G., & Blamont, J. E. (1977). Laser sounding of atmospheric sodium interpretation in terms of global atmospheric parameters. *Planetary and Space Science*, *25*, 1093–1109. [https://doi.org/10.1016/0032-0633\(77\)90085-X](https://doi.org/10.1016/0032-0633(77)90085-X)
- Molod, A., Takacs, L., Suarez, M., & Bacmeister, J. (2015). Development of the GEOS-5 atmospheric general circulation model: Evolution from MERRA to MERRA2. *Geoscientific Model Development*, *8*, 1339–1356. <https://doi.org/10.5194/gmd-8-1339-2015>
- Nesvorný, D., Janches, D., Vokrouhlický, D., Pokorný, P., Botke, W. F., & Jenniskens, P. (2011). Dynamical model for the Zodiacal Cloud and sporadic meteors. *The Astrophysical Journal*, *743*, 129. <https://doi.org/10.1088/0004-637X/743/2/129>
- Picone, J. M., Hedin, A. E., Drob, D. P., & Aikin, A. C. (2002). NRLMSISE-00 empirical model of the atmosphere: Statistical comparisons and scientific issues. *Journal of Geophysical Research*, *107*, 1468. <https://doi.org/10.1029/2002ja009430>
- Plane, J. M. C. (2003). Atmospheric chemistry of meteoric metals. *Chemical Reviews*, *103*, 4963–4984. <https://doi.org/10.1021/cr0205309>
- Plane, J. M. C. (2004). A time-resolved model of the mesospheric Na layer: Constraints on the meteor input function. *Atmospheric Chemistry and Physics*, *4*, 627–638. <https://doi.org/10.5194/acp-4-627-2004>
- Plane, J. M. C., Feng, W., & Dawkins, E. C. M. (2015). The mesosphere and metals: Chemistry and changes. *Chemical Reviews*, *115*, 4497–4541. <https://doi.org/10.1021/cr500501m>
- Plane, J. M. C., Feng, W., Gómez Martín, J. C., Gerding, M., & Raizada, S. (2018). A new model of meteoric calcium in the mesosphere and lower thermosphere. *Atmospheric Chemistry and Physics*, *18*, 14799–14811. <https://doi.org/10.5194/acp-18-14799-2018>
- She, C. Y., Chen, S., Hu, Z., Sherman, J., Vance, J. D., Vasoli, V., et al. (2000). Eight-year climatology of nocturnal temperature and sodium density in the mesopause region (80 to 105 km) over Fort Collins, Co (41°N, 105°W). *Geophysical Research Letters*, *27*, 3289–3292. <https://doi.org/10.1029/2000GL003825>
- Simonich, D. M., Clemesha, B. R., & Kirchhoff, V. W. J. H. (1979). The mesospheric sodium layer at 23°S: Nocturnal and seasonal variations. *Journal of Geophysical Research*, *84*, 1543–1550. <https://doi.org/10.1029/JA084iA04p01543>
- States, R. J., & Gardner, C. S. (1999). Structure of the mesospheric Na layer at 40°N latitude: Seasonal and diurnal variations. *Journal of Geophysical Research*, *104*, 11783–11798. <https://doi.org/10.1029/1999JD900002>
- Wang, Z., Yang, G., Wang, J., Yue, C., Yang, Y., Jiao, J., et al. (2017). Seasonal variations of meteoric potassium layer over Beijing (40.41°N, 116.01°E). *Journal of Geophysical Research: Space Physics*, *122*, 2106–2118. <https://doi.org/10.1002/2016ja023216>
- Wu, F., Zheng, H., Yang, Y., Cheng, X., Li, F., Du, L., et al. (2021). Lidar observations of the upper atmospheric nickel layer at Beijing (40°N, 116°E). *Journal of Quantitative Spectroscopy and Radiative Transfer*, *260*, 107468. <https://doi.org/10.1016/j.jqsrt.2020.107468>
- Yi, F., Yu, C., Zhang, S., Yue, X., He, Y., Huang, C., et al. (2009). Seasonal variations of the nocturnal mesospheric Na and Fe layers at 30°N. *Journal of Geophysical Research*, *114*. <https://doi.org/10.1029/2008JD010344>
- Yuan, T., Feng, W., Plane, J. M. C., & Marsh, D. R. (2019). Photochemistry on the bottom side of the mesospheric Na layer. *Atmospheric Chemistry and Physics*, *19*, 3769–3777. <https://doi.org/10.5194/acp-19-3769-2019>